

Calibration of vertical array tilt using snapping shrimp sound

Zhuqing Yuan, Edward L. Richards, H. C. Song, W. S. Hodgkiss, and Shefeng Yan

Citation: [The Journal of the Acoustical Society of America](#) **144**, 1203 (2018); doi: 10.1121/1.5054089

View online: <https://doi.org/10.1121/1.5054089>

View Table of Contents: <https://asa.scitation.org/toc/jas/144/3>

Published by the [Acoustical Society of America](#)

ARTICLES YOU MAY BE INTERESTED IN

[Estimating relative channel impulse responses from ships of opportunity in a shallow water environment](#)

[The Journal of the Acoustical Society of America](#) **144**, 1231 (2018); <https://doi.org/10.1121/1.5052259>

[Acoustic scattering comparison of Kirchhoff approximation to Rayleigh-Fourier method for sinusoidal surface waves at low grazing angles](#)

[The Journal of the Acoustical Society of America](#) **144**, 1269 (2018); <https://doi.org/10.1121/1.5052256>

[Real-time tracking of a surface ship using a bottom-mounted horizontal array](#)

[The Journal of the Acoustical Society of America](#) **144**, 2375 (2018); <https://doi.org/10.1121/1.5064791>

[Performance comparisons of array invariant and matched field processing using broadband ship noise and a tilted vertical array](#)

[The Journal of the Acoustical Society of America](#) **144**, 3067 (2018); <https://doi.org/10.1121/1.5080603>

[Compressive sensing method to leverage prior information for submerged target echoes](#)

[The Journal of the Acoustical Society of America](#) **144**, 1406 (2018); <https://doi.org/10.1121/1.5053698>

[Head waves in ocean acoustic ambient noise: Measurements and modeling](#)

[The Journal of the Acoustical Society of America](#) **143**, 1182 (2018); <https://doi.org/10.1121/1.5024332>



**Advance your science and career
as a member of the**

ACOUSTICAL SOCIETY OF AMERICA

LEARN MORE



Calibration of vertical array tilt using snapping shrimp sound

Zhuqing Yuan,^{1,a),b)} Edward L. Richards,¹ H. C. Song,¹ W. S. Hodgkiss,¹ and Shefeng Yan^{2,b)}

¹*Scripps Institution of Oceanography, La Jolla, California 92093-0238, USA*

²*Institute of Acoustics, Chinese Academy of Sciences, Beijing, 100190, China*

(Received 25 April 2018; revised 7 August 2018; accepted 12 August 2018; published online 7 September 2018)

Snapping shrimp are the dominant biological source of high-frequency (>2 kHz) ambient noise in warm coastal waters. In a recent experiment, the highly impulsive signals produced by shrimp snaps were recorded continually by a large-aperture vertical array (56 m) that was bottom-moored in 100-m deep shallow water. Assuming the array vertical, initial localization of individual snaps based on wavefront curvature along the array indicated that all snaps came from either above or beneath the flat seabed. By constraining all snaps to originate from the seabed, several hundred snaps within a radius of 500 m from the array over a 20-s window were detected successfully and localized in the three-dimensional space of time-of-arrival, range, and array tilt. Since the estimated array tilt for each snap is a projection of the absolute array tilt onto the nominal array-snap plane, the maximal tilt in the range and tilt domain corresponds to the absolute array tilt. Both simulations and data demonstrate that snapping shrimp can be exploited as a source of opportunity for calibration of vertical array tilt. © 2018 Acoustical Society of America. <https://doi.org/10.1121/1.5054089>

[SED]

Pages: 1203–1210

I. INTRODUCTION

Snapping shrimp are small creatures (e.g., 3–5 cm) that thrive in shallow waters usually less than 60 m deep and warmer than 11 °C, forming colonies on or near the seabed in interstices of structures such as rock, debris, and coral.^{1,2} A significant feature of snapping shrimp is one enlarged claw, which produces highly impulsive noise, known as snaps, via the collapse of cavitation bubbles during the rapid closure of their claws.³ Snaps accumulated by a large number of snapping shrimp can be heard as crackling sounds, dominating the high frequency (>2 kHz) soundscape in temperate and tropical coastal waters.^{2,4}

While the episodic, strong impulsive noise can be a nuisance to high-frequency sonar and acoustic communication systems, snapping shrimp can be exploited as a source of opportunity (or acoustic illumination) for passive remote sensing. The acoustic daylight (ADONIS) developed in the early 1990s was the first acoustic camera to image targets illuminated primarily by snapping shrimp noise.^{5,6} The second-generation acoustic camera (ROMANIS) was subsequently developed at the National University of Singapore, which was able to estimate the range of an imaged object once the rough location of the illuminating snapping shrimp was determined.⁷ Coral reefs are home to various living creatures including snapping shrimp,⁸ and the spatial and temporal distribution of sounds around coral reefs can be useful for monitoring their ecological health.^{9,10} Further, a snap reflected off the seabed contains information about sediment properties.¹¹ These applications require accurate localization of individual snaps or events.

Since snapping shrimp are rarely observed in water depths greater than 60 m, most studies of snapping shrimp to

date have been conducted in very shallow waters (<20 m) around harbors or coral reefs using either a single hydrophone or a small-aperture array (a few meters). In our recent acoustic experiment, however, unexpected snapping shrimp noise was recorded continuously by a large-aperture vertical array (56 m) that was deployed in about 100-m deep shallow water with a relatively flat sandy bottom.¹² The wavefront curvature along the vertical array allows for individual snaps within a radius of about 500 m (i.e., in the near field) to be localized in the two-dimensional (2-D) ambiguity surface of range and depth, similar to matched-field processing.¹³ An initial analysis, however, indicated that a lot of snaps apparently came from tens of meters above or beneath the flat seabed, even though there were no reefs or structures in the surrounding area that would have provided a shelter for snapping shrimp. A separate study involving a ship of opportunity¹⁴ has reported that the same vertical array was tilted a few degrees due to strong currents in the region. Assuming that snapping shrimp live on the flat seabed, snaps can be localized instead in the 2-D ambiguity surface of range and array tilt, with the primary focus on the array tilt. The objective of this paper is to demonstrate that snapping shrimp can serve as natural sound sources to extract vertical array tilt.

The paper is organized as follows. Section II describes the shallow water experiment conducted in the northeastern East China Sea (ECS), providing temporal and spectral characteristics of snapping shrimp noise. In Sec. III, the array processing method based on spherical-wave beamforming is described in detail, including the impact of array tilt, which is then applied to coarse localization of individual snaps that overlap in time and space. In Sec. IV, the localization results in the range and tilt domain are further enhanced by refinement post-processing using both simulations and data, from which the vertical array tilt is estimated.

^{a)}Electronic mail: z9yuan@ucsd.edu

^{b)}Also at: University of Chinese Academy of Sciences, Beijing, 100190, China.

II. THE SAVEX15 EXPERIMENT

The shallow-water acoustic variability experiment (SAVEX15) was conducted in the northeastern ECS in May 2015 using the R/V Onnuri.^{12,14} The goal of SAVEX15 was to collect acoustic and environmental data appropriate for studying the coupling of oceanography, acoustics, and underwater communications in the region. The experimental site had a nearly flat sandy bottom and water depth of approximately 100 m. Both fixed and towed source transmissions were carried out to moored vertical line arrays (VLAs) over ranges of 1–10 km. The acoustic transmissions were in various frequency bands (0.5–32 kHz), including both channel probing waveforms and communication sequences. Environmental data included water column sound speed structure, sea surface directional wave field, local wind speed and direction, and currents.

While snapping shrimp sounds were observed continuously throughout the experiment, we will analyze two segments of data (20-s long) collected during a source-tow run conducted on JD 145 (May 25): 15:43 and 16:23 UTC.¹⁴ The schematic of the experiment is illustrated in Fig. 1. The bottom-moored VLA consisted of 16 elements, equally spaced at 3.75 m, which spanned the water column from 25 to 81 m in about 100-m deep water. The sound speed profile (SSP) displayed in Fig. 1(a) is from a CTD (conductivity, temperature, and depth) profile collected on JD 145, featuring an asymmetrical underwater sound channel with the channel axis at about 40 m depth. The R/V Onnuri was towing two broadband sources (3–10 kHz and 12–32 kHz) simultaneously at a speed of 3 knots (1.5 m/s) along a ship track. Thus, the VLA recorded waveforms broadcast from the towed sources at a mid-depth (50-m) as well as snapping shrimp sounds. The sampling frequency was $f_s = 100$ kHz, and a high-pass filter with a cutoff frequency at 500 Hz was applied to suppress shipping noise.

An example of a 10-s time series received by the bottom-most hydrophone at 81 m (#16) is shown in Fig. 2. The episodic, highly impulsive signals are due to snapping shrimp. Also plotted is a close-up single snap (gray), whose

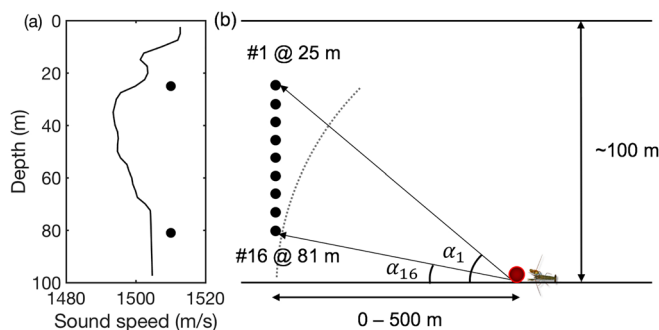


FIG. 1. (Color online) Schematic of the VLA and sound speed structure on JD 145 (May 25) during SAVEX15. (a) SSP from a CTD cast on JD145, featuring an underwater sound channel with the channel axis at 40 m depth. (b) A 16-element, 56-m long VLA was bottom-moored in approximately 100-m deep water. For snapping shrimp on the flat seabed, the wavefront curvature along the array permits localization of individual snaps within a radius of 500 m, with α_i representing the grazing angle from a shrimp to the i th element of the array.

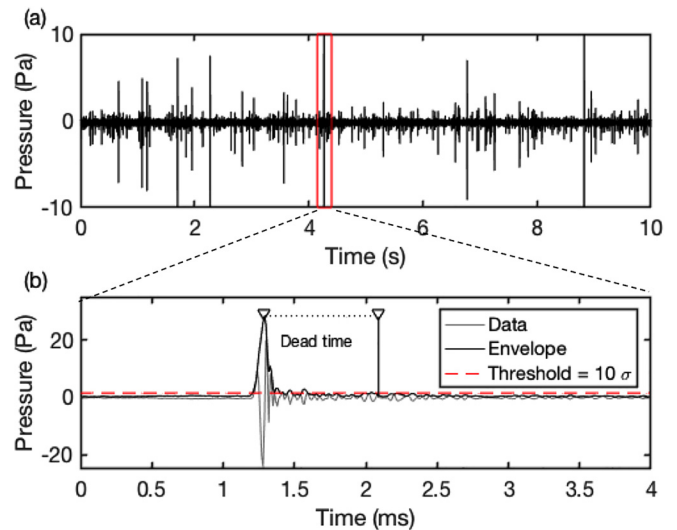


FIG. 2. (Color online) (a) An example of a 10-s time series received by the bottom-most hydrophone of the VLA at 81 m (#16), showing episodic, impulsive signals attributed to snapping shrimp. (b) Close-up of a single snap (gray) and its envelope (black). The main pulse duration is less than 150 μ s with the peak-to-peak level of about 153 dB *re* 1 μ Pa. Note that the time series in (a) is clipped.

main pulse duration is less than 150 μ s with the peak-to-peak level of about 153 dB *re* 1 μ Pa. Following the peak are small oscillations lasting about 1.6 ms (i.e., coda). The spectral density from a 1-min data segment (JD145 15:43) is shown in Fig. 3 for all 16 elements of the VLA from 1 to 40 kHz. The three spectral peaks at 5, 7, and 9 kHz are tonal signals broadcast by the lower frequency towed source. The higher frequency towed source (12–32 kHz) was not broadcasting at the time. In the absence of snapping shrimp, the ambient-noise spectral density tends to decrease continuously with an increasing frequency, as indicated by the dashed line.⁵ Thus, the higher spectral energy at frequencies above 10 kHz (marked by a circle) can be attributed to snapping shrimp noise.

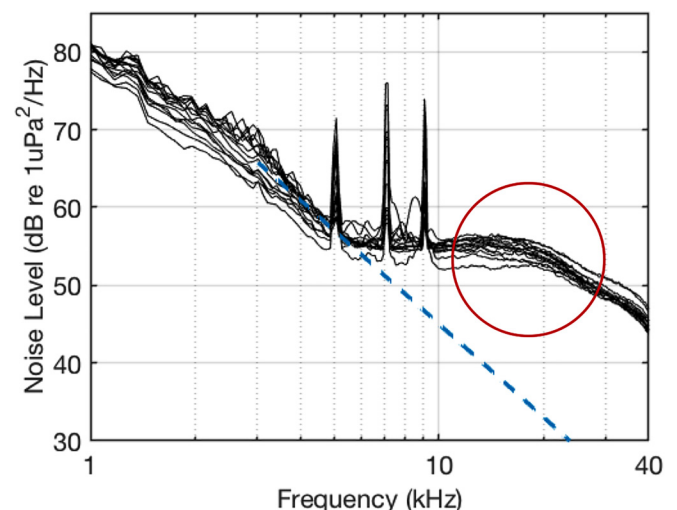


FIG. 3. (Color online) Spectral density from a 1-min data segment (JD145 15:43) across the 16-element VLA (1–40 kHz). The three spectral peaks at 5, 7, and 9 kHz are tonal signals broadcast by the towed source at 50-m depth. The higher spectral energy at frequencies above 10 kHz (marked by a circle) can be attributed to snapping shrimp noise.

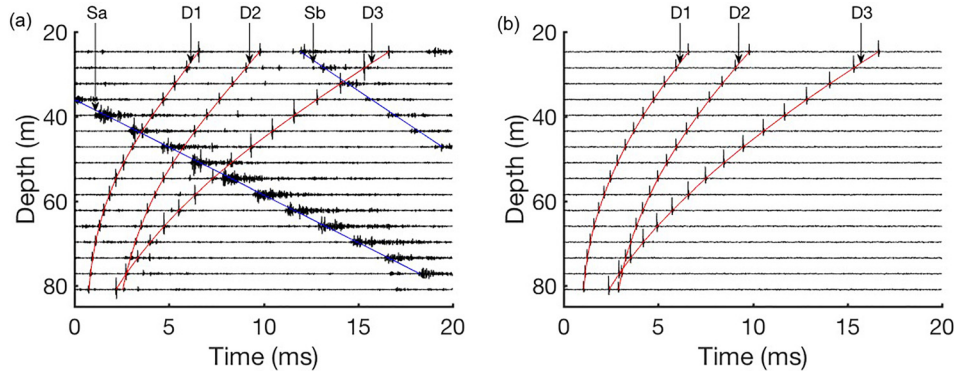


FIG. 4. (Color online) Arrival structure of snapping shrimp noise: (a) data and (b) simulation. (a) Waterfall plot of 20-ms data received on the VLA (16:53:01 UTC). A high-pass filter with a cutoff frequency at 9 kHz was applied to remove the tonal signals in Fig. 3. There are three snaps (direct arrivals) captured, denoted by D1, D2, and D3. The spherical wavefronts based on the estimated snap locations are superimposed by curves. In addition, there are two non-impulsive (dispersive) arrivals, denoted by Sa and Sb, which are propagating downward (lines). (b) Simulated waterfall plot with three direct arrivals (D1, D2, and D3) corresponding to (a).

An example of the arrival structure of snapping shrimp noise along the VLA is illustrated in Fig. 4(a). A high-pass filter with a cutoff frequency at 9 kHz was applied to remove the tonal signals shown in Fig. 3. Three distinct snaps (direct arrivals) are arriving almost simultaneously in this 20-ms time window, denoted by D1, D2, and D3. The corresponding spherical wavefronts based on the estimated snap locations, which will be discussed in Sec. IV, are superimposed in curves. Also noticeable are two additional arrivals, denoted by Sa and Sb, which are propagating downward and dispersive (a few milliseconds long). They are not direct, but surface-reflected arrivals off a rough sea surface, and are not considered in this work. However, it is worth mentioning that the association of direct and surface-reflected snaps has been recently exploited for localizing snapping shrimp using a small-aperture array in very shallow water.¹⁵

III. ARRAY PROCESSING

The array processing is based on spherical-wave beamforming to localize the individual snaps that are in the near field (<500 m) and overlap in time and space, as illustrated in Fig. 4(a).

A. Signal model

Due to the impulsive nature of shrimp snap, the direct path received signal on the j th element of the VLA can be modeled as a sum of K snaps

$$s_j(t) = \sum_{k=1}^K a_{j,k} \delta(t - (t_k + \tau_{j,k})) + n_j(t), \quad j = 1, \dots, N, \quad (1)$$

where $a_{j,k}$ is the amplitude of the k th snap at the j th receiver, $\tau_{j,k}$ is a relative time delay between the source location of the k th snap and the j th receiver, with respect to the top element of the array (i.e., $\tau_{1,k} = 0$), and t_k is the time-of-arrival of the k th snap at the top element ($j = 1$). $\delta(t)$ is a Dirac-delta function, and N is the number of array elements. Given the snaps are very high level compared to the noise term $n_j(t)$, this term will be dropped for simplicity. Note that the signal model is similar

to the time-domain Green's function (or channel impulse response) in a multipath environment using ray theory.¹⁶

To detect individual snaps with large amplitudes, a threshold peak detection approach with a dead-time window¹⁷ can be applied to the envelope of the data. The threshold level is set to multiples of the standard deviation of the envelope over an extended period of time (e.g., 10σ of a 10-s data set), and the maximum value within the dead-time window is considered a significant snap. No secondary detection is made within the dead-time window following the primary detection to prevent multiple counts for the same snap, given the oscillations (tail) following the main pulse of each snap. The length of the dead-time window is chosen to ensure that pressure oscillations are lower than the threshold after the window. Here, the dead-time window is set to 0.8 ms, as illustrated in Fig. 2(b). The amplitudes at the selected detection times are reset to one, otherwise zero, such that $a_{j,k} = 1$ for all j and k in Eq. (1), generating a sparse impulse train for each VLA element. Then Eq. (1) is convolved with a symmetric, shaping or window function $w(t)$ in order to transform the impulse train to a smooth time series, $\bar{s}_j(t)$:

$$\bar{s}_j(t) = \sum_{k=1}^K w(t - (t_k + \tau_{j,k})). \quad (2)$$

The length of the window function is made less than half the dead-time to avoid overlapping of snaps in time. We choose a Hanning window of 21 samples (i.e., 1/4 of the dead-time), while other types of windows (e.g., Hamming or Kaiser) are equally applicable.

Finally, a delay-and-sum beamformer output using a vertical array is given by

$$\begin{aligned} B(t, r, d) &= \sum_{j=1}^N \bar{s}_j(t + \hat{\tau}_j(r, d)) \\ &= \sum_{k=1}^K \sum_{j=1}^N w(t - (\tau_{j,k} + t_k) + \hat{\tau}_j(r, d)), \end{aligned} \quad (3)$$

where $\hat{\tau}_j(r, d)$ is a replica (model) time delay calculated for a possible source located at range (r) and depth (d), which is

defined with respect to the top element (i.e., $\hat{\tau}_1(r, d) = 0$). For snaps originating from the seabed, d reduces to the water depth, D .

B. Impact of array tilt

While we want to keep an array vertical, it is almost impossible to avoid a small tilt in practice due to currents and tides. This is especially true in the ECS known for strong tidal currents.¹² Indeed, a recent study¹⁴ has found that the same vertical array is tilted about 3° towards the northwest, consistent with the acoustic current Doppler profile (ADCP) data and a regional ocean model.¹⁸ The impact of array tilt can be significant for spherical-wave beamforming, which depends on the wavefront curvature in the near field. In fact, our beamformer output using Eq. (3) indicated that the localized snaps appear to come from either above or beneath the seafloor (i.e., $d \neq D$), when the array tilt is not accommodated.

The impact of the array tilt is illustrated in Fig. 5. The vertical array is bottom-moored at the origin and tilted θ_0 (clockwise) in the $x=0$ plane (A). A source snap (S) is located in the $z=0$ plane (i.e., seabed) at range (r) with an azimuth angle (φ) from the positive x axis. For a small tilt angle (e.g., $\theta_0 \leq 5^\circ$), the apparent tilt angle viewed from the nominal array-snap plane (dashed line) is a projection of the absolute array tilt (from A to A'), such that $\theta \approx \theta_0 \sin \varphi$. Representative examples of snaps coming from various azimuth angles (φ) are shown in Fig. 5(b). Note that in the coordinate system defined in Fig. 5(a), the z -axis is pointing upwards from the seafloor. Thus, the depth of an array element is $d_j = D - z_j$. A slight change in the array depth due to array tilt is negligible for a small array tilt.

Assuming that snaps originate from the flat seabed ($d = D$), the beamformer of Eq. (3) can be rewritten as

$$B(t, r, \theta) = \sum_{k=1}^K \sum_{j=1}^N w((t - t_k) - (\tau_{j,k} - \hat{\tau}_j(r, \theta))), \quad (4)$$

where $\hat{\tau}_j(r, \theta)$ is a replica time delay calculated for a source located at range (r) along the seabed in the presence of array tilt θ .

IV. LOCALIZATION OF SNAPPING SHRIMP

In this section, we evaluate the beamformer of Eq. (4) for the 20-ms data shown in Fig. 4(a). We will construct the 3-D ambiguity surface in (t, r, θ) , which then reduces to the 2-D ambiguity surface in (r, θ) . The ambiguity surface is also compared to the one from the simulated data in Fig. 4(b). The replica time delays, $\hat{\tau}_j(r, \theta)$, will incorporate the sound speed variation along the path, while ignoring the ray bending (refraction) in the near field. The resulting coarse estimation will be enhanced by refinement post-processing. The analysis is extended via automation to two segments of 20-s data for 2-D range and tilt estimation, from which the absolute array tilt will be extracted.

A. Ambiguity surface

As described in Sec. II, the array processing involves a high-pass filter to remove the three tonal signals, envelope detection with thresholding (10σ) and dead-time (0.8 ms), normalization, and smoothing by a shaping function (0.2 ms). To construct the 3-D ambiguity surface of Eq. (4), the replica time delays are computed using a simple ray model incorporating the sound speed variation along the path with no ray bending (i.e., straight line),¹⁶

$$\hat{\tau}_j(r, \theta) = \frac{1}{\sin \alpha_j} \int_0^{z_j} \frac{1}{c(z)} dz, \quad (5)$$

with

$$\tan \alpha_j = z_j / (r - z_j \tan \theta). \quad (6)$$

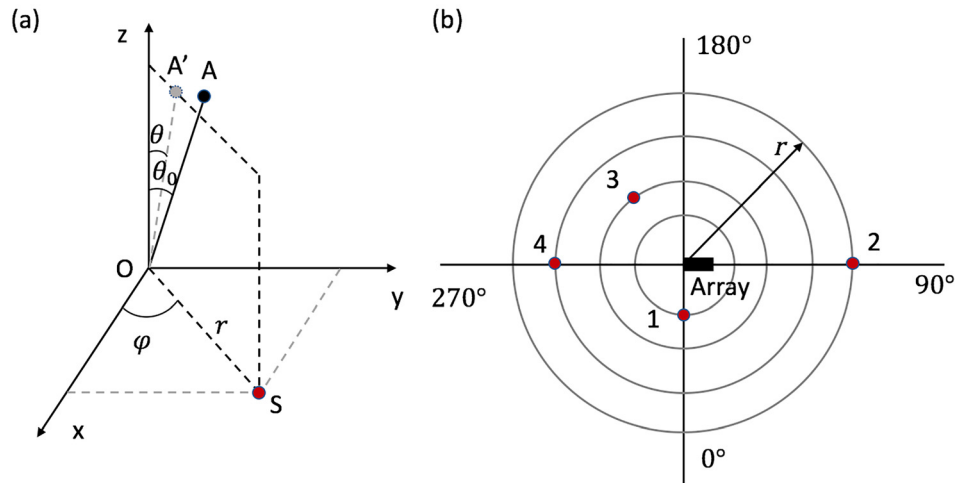


FIG. 5. (Color online) (a) Geometry of the array (A) with respect to a source (S). The vertical array at the origin is tilted θ_0 (clockwise) in the $x=0$ plane (A), while the source snap (S) is located in the $z=0$ plane (i.e., seabed) with an azimuth angle φ . For a small tilt (e.g., $\theta_0 \leq 5^\circ$), the apparent tilt angle in the nominal source-array plane (dashed line) is a projection of the absolute array tilt, i.e., $\theta \approx \theta_0 \sin \varphi$. (b) Top view with 0° corresponding to the positive x axis. The tilted VLA is denoted by a solid rectangle, and the four snaps (dots) are distributed at various ranges (r) and azimuth angles (φ). The projected tilt angles for Snaps 2 and 4 are θ_0 and $-\theta_0$, respectively, while $\theta = 0$ for Snap 1.

Note that α_j is the grazing angle of the direct ray path from the source in the $z=0$ plane (seabed) to the array element at z_j , as depicted in Fig. 1(b).

The beamformer output in the 3-D parameter space of (t, r, θ) for the 20-ms data shown in Fig. 4(a) is presented in Fig. 6(a). The three clusters of direct snaps (D1, D2, and D3) are well separated in the 3-D ambiguity surface, corresponding to the three wavefronts in Fig. 4(a). The 2-D surfaces sliced at the estimated time-of-arrival at the top element (t_1 , t_2 , and t_3) of D1, D2, and D3 from the 3-D surface are superimposed and normalized, generating the 2-D ambiguity surface in (r, θ) , which is displayed in Fig. 6(c). The estimated range and tilt (peak) is denoted by white circles: D1 = (217 m, 3.9°), D2 = (224 m, 1.2°), and D3 = (134 m, -3.8°). The mainlobe structure of the ambiguity surface is far from being ideal with an inherent elongated shape widened by the shaping function. The temporal resolution is further reduced by the envelope peak detection. For example, for direct path D2, the 3-dB mainlobe width is 2.7° in tilt and 40 m in range. In this multi-source problem, any sidelobes from other sources can negatively impact the estimation results for a given snap. To improve the 2-D range and tilt estimation, the idea of additional post-processing is primarily to isolate and localize every single snap with a smaller grid size, as described in Sec. IV B.

B. Refinement processing

First, a given snap is isolated and its wavefront is extracted. The 3-D ambiguity surface provides initial estimates of parameters $(\hat{t}_k, \hat{r}_k, \hat{\theta}_k)$ for K snaps, from which we can calculate the crossing times of each wavefront along the array (Fig. 4, curves), i.e., $\hat{t}_{j,k} = \hat{t}_k + \hat{\tau}_j(\hat{r}_k, \hat{\theta}_k)$, for $j = 1, \dots, N$. However, it is not likely that the resulting modeled wavefront coincides with the snap peaks, due to the limited resolution in range and tilt along with environmental mismatch in the model. Thus, for each coarse estimate, a more accurate wavefront ($\tilde{t}_{j,k}$) can be extracted by finding the nearest snap peak of the estimated wavefront ($\hat{t}_{j,k}$) in each of the array element:

$$\tilde{t}_{j,k} = \arg \min_{\{i\}} |t_{j,i} - \hat{t}_{j,k}|, \quad j = 1, \dots, N, \quad (7)$$

where the time index $\{i\}$ is searched in the vicinity of the wavefront crossing, $\hat{t}_{j,k}$. If the difference $|t_{j,i} - \hat{t}_{j,k}|$ is too large (e.g., over half of the dead-time window or 40 samples), $\tilde{t}_{j,k}$ is not considered reliable and the corresponding element will be excluded in the refinement processing below. Note that the refined time-of-arrival on the top element $\tilde{t}_{1,k}$ becomes \tilde{t}_k .

The next step is to search for a refined estimate of the range and tilt, $(\tilde{r}_k, \tilde{\theta}_k)$, by minimizing the mean-squared-

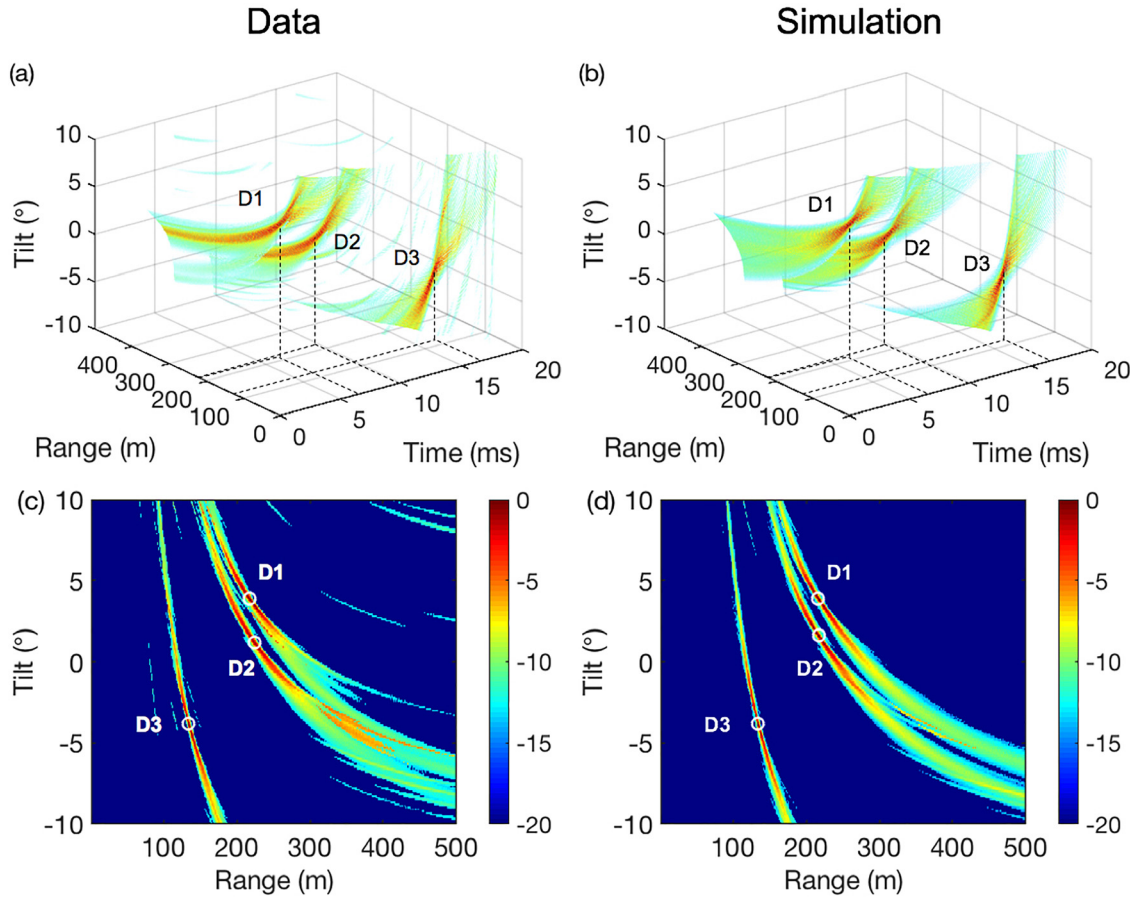


FIG. 6. (Color online) Ambiguity surface $|B|^2$ (dB) in the 3-D parameter space of time (t), range (r) and tilt (θ): (a) data and (b) simulation, corresponding to Figs. 4(a) and 4(b), respectively. The three direct snaps (D1, D2, and D3) are well-separated in the 3-D ambiguity surface, and there is an excellent agreement between data and simulation. Panels (c) and (d) show the 2-D ambiguity surface in (r, θ) where the 2-D range-tilt surfaces sliced at the time-of-arrival (t_1 , t_2 , t_3) from the 3-D plots (top) are superimposed and normalized. The three peaks in the range-tilt ambiguity surface are denoted by white circles. The dynamic range is 15 dB in (a) and (b), and 20 dB in (c) and (d).

error (MSE) between the revised ($\tilde{t}_{j,k}$) and the replica time delays,

$$(\tilde{r}_k, \tilde{\theta}_k) = \arg \min_{(r, \theta)} \frac{1}{N} \sum_{j=1}^N |(\tilde{t}_{j,k} - \tilde{t}_{1,k}) - \hat{\tau}_j(r, \theta)|^2. \quad (8)$$

Since the replica time delays $\hat{\tau}_j(r, \theta)$ need to be evaluated repeatedly, in practice it is much more efficient to compute them once and save them in a library. Further, a smaller grid size can be afforded here in generating the replica time delays $\hat{\tau}_j(r, \theta)$ in Eq. (8).

C. Numerical simulations

Given the uncertainty associated with the data and replicas, we also generated simulated data containing the three direct snaps identified after refinement processing, as presented earlier in Fig. 4(b): D1 = (216 m, 3.9°), D2 = (217 m, 1.6°), and D3 = (134 m, -3.8°). The source signal is assumed an exponentially damped sinusoid at 30 kHz. The 3-D ambiguity surface for the simulated data is illustrated in Fig. 6(b), showing an excellent agreement with the data shown in Fig. 6(a). The three clusters of direct snaps (D1, D2, and D3) are well separated. The wavefronts estimated

from the localization results of the three snaps are superimposed in Fig. 4(b). The 2-D ambiguity surface in (r, θ) is also displayed in Fig. 6(d), from which the range and tilt are estimated: D1 = (214 m, 4.0°), D2 = (217 m, 1.6°), and D3 = (134 m, -3.8°). After refinement processing, the estimates of range and tilt remain the same except for D1 = (216 m, 3.9°), which are identical to those assumed in the simulated data.

D. Range and tilt estimation

The entire process can be fully automated to analyze a much longer data set. We have chosen two sets of 20-s data separated by 40 min and localized the snaps in the 2-D range and tilt domain, which are displayed in Figs. 7(a) and 7(c). The number of snaps captured in the data is (a) 567 and (c) 883. As illustrated in Fig. 5(a), the tilt angle is a projection of the absolute array tilt onto the nominal array-snap plane, and thus the maximal array tilt determined by the boundaries indicates the absolute array tilt. The absolute tilt angles are found to be approximately (a) 2° and (c) 3.2° (lines), respectively, using snaps detected at ranges greater than 100 m. The snaps at closer ranges (i.e., <100 m) are sensitive to

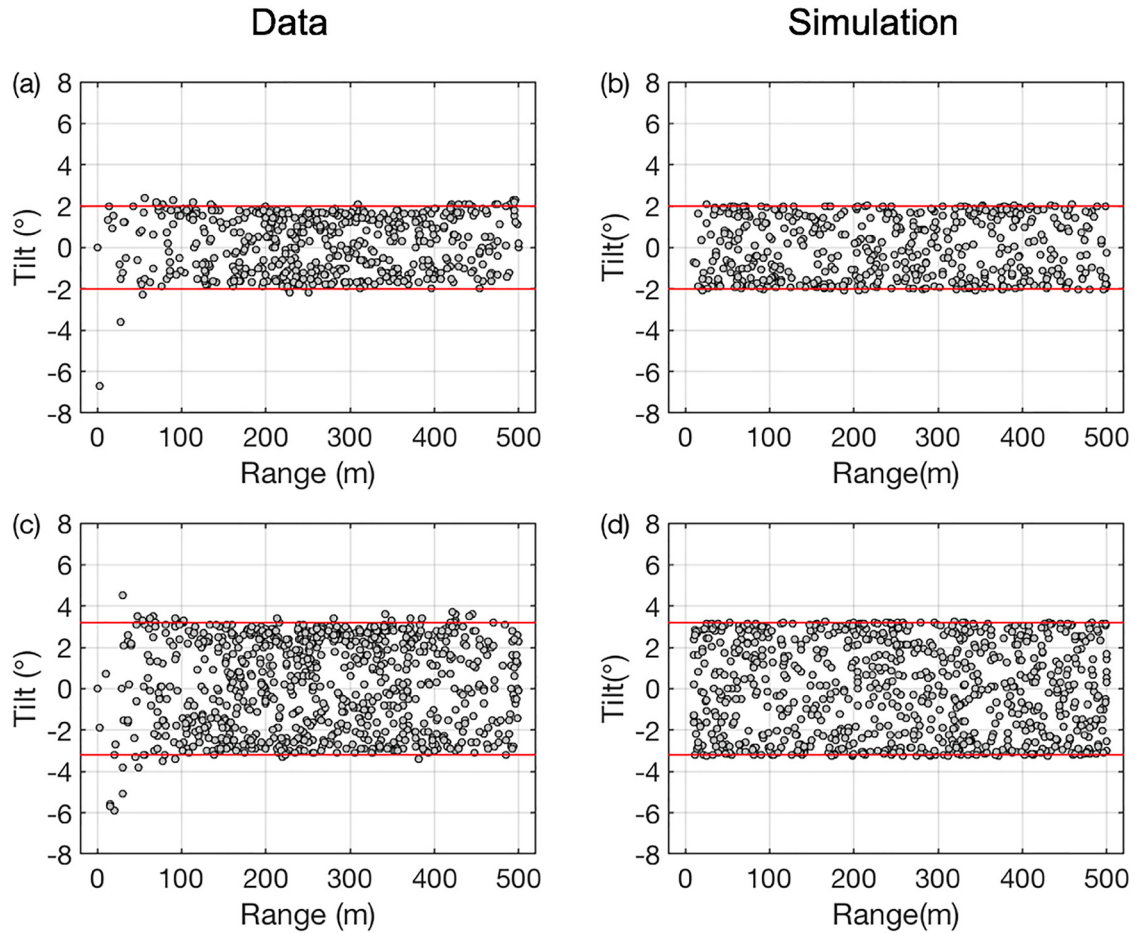


FIG. 7. (Color online) 2-D parameter estimation results in range and tilt for two sets of 20-s experimental data (left column) and the corresponding simulated data (right column). The number of snaps captured in the data is (a) 567 and (c) 883. The absolute (maximum) array tilt angles at the boundaries (denoted by lines) are approximately (a) 2° and (c) 3.2°, respectively, using snaps detected at ranges greater than 100 m. For simulations, the number of snaps included is (b) 500 and (d) 800, which are randomly distributed in range (10–500 m) and azimuth angle (0°–360°). There is an excellent agreement between data and simulations in terms of the maximum array tilt.

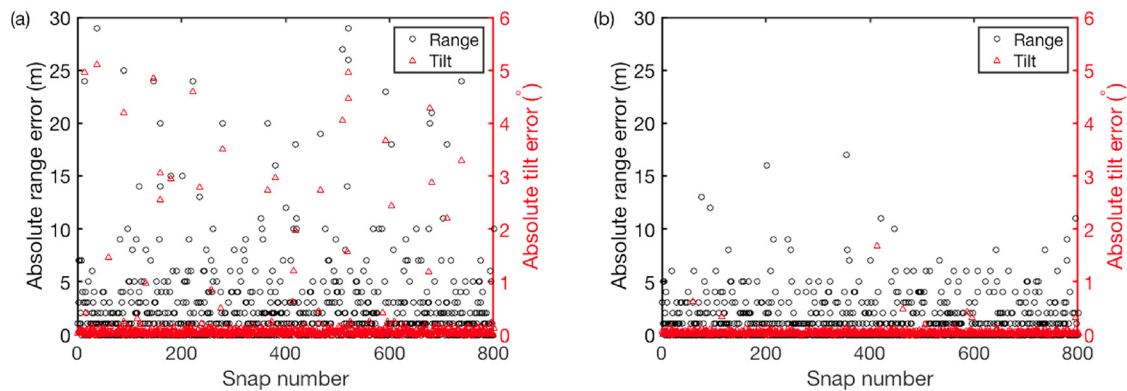


FIG. 8. (Color online) Absolute error for the range (\circ) and tilt (Δ) estimation: (a) before and (b) after refinement processing for the simulated data shown in Fig. 7(d). The horizontal axis is the snap number. The left- and right-side vertical axes denote range and tilt error, respectively.

mismatch in sound speed and water depth, and thus are not considered for array calibration purposes.

To validate the experimental results, two sets of simulated data are generated with the absolute array tilt of 2° and 3.2° in Figs. 7(b) and 7(d), respectively. The number of snaps included are (b) 500 and (d) 800, which are randomly distributed in range (10–500 m) and azimuth angle (0° – 360°). There is an excellent agreement between data and simulations in terms of the maximum array tilt.

Finally, Fig. 8 shows the absolute error for range (\circ) and tilt (Δ) estimation: (a) before and (b) after refinement processing for the simulated data shown in Fig. 7(d). The horizontal axis denotes the snap number, while the left- and right-side vertical axes represent range error and tilt error, respectively. After the refinement processing, the mean absolute errors of the localization results in Figs. 7(b) and 7(d) have reduced from [2.57 m, 0.20°] to [1.07 m, 0.025°] and from [2.48 m, 0.16°] to [1.31 m, 0.034°], respectively. Clearly, the absolute tilt error (Δ) is much smaller with remarkable reduction of outliers after refinement processing. The simulation results confirm that the refinement processing significantly improves the localization accuracy in the range and tilt domain.

V. SUMMARY

Snapping shrimp typically found in very shallow waters (<20 m) were observed continually in 100-m deep shallow water by a vertical array during the SAVEX15. The wavefront curvature along the array allowed for localization of individual snapping shrimp within a radius of 500 m from the array. Preliminary analysis assuming no array tilt indicated that the snaps apparently originated from either above or below the seafloor. A separate study using ship noise has reported that the same vertical array was tilted about 3° due to strong tidal currents in the region. The array tilt then was incorporated into the 3-D parameter space of time-of-arrival, range, and tilt, while constraining the snaps to the seabed. The primary focus in this work was on 2-D estimation in range and tilt, from which the absolute array tilt was estimated. Due to the impulsive nature of snaps, a series of array processing steps involved thresholding, normalization and

shaping, beamforming, and refinement. We analyzed two sets of 20-s long data and obtained array tilts of 2° and 3.2° , which are similar to the 3° reported in Ref. 14. The simulation results showed an excellent agreement with the data, suggesting that snapping shrimp can be used as sources of opportunity for calibration of vertical array tilt in shallow water.

ACKNOWLEDGMENTS

This work is supported by the U.S. Office of Naval Research. Z.Y. is partially funded by the UCAS Joint Ph.D. Training Program.

- ¹M. W. Johnson, F. A. Everest, and R. W. Young, "The role of snapping shrimp (Crangon and Synalpheus) in the production of underwater noise in the sea," *Biol. Bull.* **93**, 122–138 (1947).
- ²F. A. Everest, R. W. Young, and M. W. Johnson, "Acoustical characteristics of noise produced by snapping shrimp," *J. Acoust. Soc. Am.* **20**, 137–142 (1948).
- ³M. Versluis, B. Schmitz, A. von der Heydt, and D. Lohse, "How snapping shrimp snap: Through cavitating bubbles," *Science* **289**, 2114–2117 (2000).
- ⁴D. H. Cato and M. J. Bell, "Ultrasonic ambient noise in Australian shallow waters at frequencies up to 200 kHz," Material Research Laboratory Technical Report No. MRL-TR91-23, Ascot Vale, Victoria, 1992.
- ⁵M. J. Buckingham, B. V. Berkout, and S. A. Glegg, "Imaging the ocean with ambient noise," *Nature (London)* **356**, 327–329 (1992).
- ⁶C. L. Epifanio, J. R. Potter, G. B. Deane, M. L. Readhead, and M. J. Buckingham, "Imaging in the ocean with ambient noise: The ORB experiments," *J. Acoust. Soc. Am.* **106**, 3211–3225 (1999).
- ⁷M. Chitre, S. Kuselan, and V. Pallayil, "Ambient noise imaging in warm shallow waters; robust statistical algorithms and range estimation," *J. Acoust. Soc. Am.* **132**, 838–847 (2012).
- ⁸S. Simpson, M. Meekan, J. Montgomery, R. McCauley, and A. Jeffs, "Homeward sound," *Science* **308**(5719), 221–221 (2005).
- ⁹S. E. Freeman, M. J. Buckingham, L. A. Freeman, M. O. Lammers, and G. L. D'Spain, "Cross-correlation, triangulation, and curved-wavefront focusing of coral reef sound using a bi-linear hydrophone array," *J. Acoust. Soc. Am.* **137**, 30–41 (2015).
- ¹⁰M. Lammers, W. A. R. E. Brianard, T. Mooney, and K. Wong, "An ecological acoustic recorder (EAR) for long-term monitoring of biological and anthropogenic sounds on coral reefs and other marine habitats," *J. Acoust. Soc. Am.* **123**(5), 1720–1728 (2008).
- ¹¹M. Chitre, T. Koay, and J. Potter, "Origins of directionality in snapping shrimp sounds and its potential applications," in *Proc. IEEE OCEANS Conf.* (2003), Vol. 2, pp. 889–896.
- ¹²H. C. Song, C. Cho, W. S. Hodgkiss, S.-H. Nam, S.-M. Kim, and B.-N. Kim, "Underwater sound channel in the northeastern East China Sea," *Ocean Eng.* **147**, 370–374 (2018).

- ¹³A. Baggeroer, W. Kuperman, and P. Mikhalevsky, "An overview of matched field methods in ocean acoustics," *IEEE J. Oceanic Eng.* **18**, 401–424 (1993).
- ¹⁴G. Byun, C. Cho, H. C. Song, J. S. Kim, and S.-H. Byun, "Array invariant-based calibration of array tilt using a source of opportunity," *J. Acoust. Soc. Am.* **143**(3), 1318–1325 (2018).
- ¹⁵Y. M. Too, M. Chitre, G. Barbastathis, and V. Pallayil, "Localizing snapping shrimp noise using a small-aperture array," *IEEE J. Oceanic Eng.* **PP**(99), 1–13 (2017).
- ¹⁶F. B. Jensen, W. A. Kuperman, M. B. Porter, and H. Schmidt, *Computational Ocean Acoustics*, 2nd ed. (Springer, New York, 2011), pp. 196–198.
- ¹⁷M. W. Legg, "Non-Gaussian and non-homogeneous Poisson models of snapping shrimp noise," Ph.D. dissertation, Curtin Univ. Technol, Perth, Australia, 2010.
- ¹⁸S. Nam, D. Kim, S. Lee, B. Kim, K. Kang, and Y. Cho, "Nonlinear internal wave spirals in the northern East China Sea," *Sci. Rep.* **8**, 3473 (2018).